fluids

MDPI

Article

Pore-Scale Lattice Boltzmann Simulation of Blind-End Oil Retention

Huiyu Wang [1,2,*], Yuegang Wang [3], Qi Lv [1], Guanghuan Wu [1] and Lijie Liu [1]

[1] Exploration and Development Research Institute, Shengli Oilfield Company, Sinopec, Dongying 257015, China
[2] Postdoctoral Scientific Research Working Station, Shengli Oilfield Company, Sinopec, Dongying 257002, China
[3] Shengli Oilfield Company, Sinopec, Dongying 257001, China
* Correspondence: t-wanghuiyu.slyt@sinopec.com

Abstract

Currently, a large number of simulation studies on multiphase flow at the pore scale are conducted based on complex porous media. As a microstructure that constitutes the porous media of reservoir, the blind-end can efficiently trap crude oil. However, the research on the multiphase flow within a blind-end is still lacking. In this paper, we used the color-gradient model to simulate the dynamic process that occurs when the oil–water interface passes through a blind-end based on the waterflooding. Furthermore, the effect of influencing factors on the oil in a blind-end (residual oil) after the oil–water interface passes the blind-end were investigated. The results show that the displacement of the water phase from a blind-end full of the oil phase can be categorized into three stages. First, the oil–water interface moves towards the blind-end. Second, when the oil–water interface reaches the blind-end, a portion the of toil phase in the blind-end can be displaced by the water phase. Third, after the oil–water interface passes through the blind-end, a portion of the oil phase (residual oil) is trapped in the blind-end. The residual oil saturation of a blind-end is defined as the ratio of the area of residual oil in a blind-end to the total area of a blind-end. The residual oil saturation in the blind-end increases with the increase in the water velocity, the oil-to-water viscosity ratio, the main channel width, and the blind-end depth. Conversely, it decreases with the increase in blind-end width. The findings provide critical insights into the oil retention mechanism in the blind-end.

Keywords: pore-scale simulation; lattice Boltzmann method; displacement process; blind-end

Check for updates

Academic Editors: Kannan N. Premnath and Jie Bao

Received: 3 January 2026
Revised: 3 February 2026
Accepted: 6 February 2026
Published: 12 February 2026

Copyright: © 2026 by the authors. Licensee MDPI, Basel, Switzerland. This article is an open access article distributed under the terms and conditions of the Creative Commons Attribution (CC BY) license.

1. Introduction

The crude oil buried underground is extremely important for the development of industry. It is not only the main source of fuels, but the primary raw material for different types of chemicals [1], as well. Generally, the production of crude oil can pass through three stages, namely primary recovery, secondary recovery, and tertiary recovery. For the stage of primary recovery, the natural energy of the reservoir, such as the gas cap, the edge or bottom water, and the dissolved gas, is the main reason to promote the flow of the crude oil in the reservoir. The duration of primary recovery is relatively short. When the primary recovery is completed there are numerous areas that are rich in crude oil in the reservoir. For the stage of secondary recovery (waterflooding process) [2], water is injected into the reservoir to maintain the reservoir pressure and to displace the crude oil. As for the stage of tertiary recovery, it mainly includes chemical flooding, miscible flooding, and other enhanced oil recovery (EOR) methods [3–5].

Compared to the other two stages, the duration of waterflooding is generally longer, mainly due to its low risk, easy operation, and cost-effectiveness [6]. Underground porous media are complex, containing types of microstructure, so the two-phase flow between water and oil in porous media is diverse as well [7].

The blind-end is a typical and widely distributed microstructure. Figure 1 is reprinted with permission from Ref. [8], published by Elsevier in 2018. It can be seen from Figure 1 that the blind-end in the red circle is like a small pit [8]. Based on the microfluidic experiment, some scholars conducted relevant experimental studies on the oil in a blind-end.



Figure 1. Crude oil in a blind-end [8].

Through a glass micromodel with heterogeneous porous media, Lv et al. found that the CO_2 foam flooding can more effectively mobilize the trapped oil in a blind-end than water [9]. Mohammadi et al. designed a microfluidic chip made of calcite with blind-ends to study the effect of waterflooding with different salinity on crude oil in blind-ends [10]. They found that the change in wettability by low-salinity water is a relatively slow process. Similarly, Du et al. developed a glass model with blind-ends and studied the effect of low-salinity waterflooding on the oil in blind-ends [11]. They also found that the change in wettability is a major mechanism.

In addition, some scholars also used the microfluidics to study the effect of different types of chemicals or chemical systems on the oil in the blind-end. For instance, Wang et al. demonstrated that the polymer (HPAM solution) is able to effectively displace more oil in a blind-end than water and glycerin [12]. In addition to the polymer, Wang et al. also found that the surfactant can displace some oil that cannot be displaced out of the blind-end by the water [13]. Yekeen et al. found that the binary system including the nanoparticle and the surfactant is effective to the oil in the blind-end [14]. Using a viscoelastic surfactant as the displacing phase, Li et al. demonstrated that the stretching effect and the replacement effect caused by this type of chemical can lead to lower oil saturation in a blind-end [15]. In the case of low IFT between two phases, Liu et al. demonstrated that the binary solution (surfactant and polymer) showed a high wash efficiency for the oil in a blind-end [16].

It can be seen from the abovementioned experimental studies that researchers primarily focused on whether chemicals can displace more crude oil from blind-ends after waterflooding, without discussing the flow behavior in the blind-end during waterflooding.

For resolving pore-scale multiphase transport phenomena, the lattice Boltzmann method (LBM) has emerged as an effective numerical approach [17–20], particularly excelling in modeling interfacial dynamics within different porous geometries. It can yield a detailed velocity field, pressure field, and saturation distribution. For multiphase flow simulations, four main models have been developed, including the color-gradient model [21,22], the pseudopotential model [23], the free energy model [24], and the phase-field model [25]. In addition to these four models, some scholars have also used the LBM to study flow phenomena at the nanoscale [26]. For instance, Yin et al. proposed a new LBM model to investigate the multiscale gas transport processes in a shale matrix–microfracture system [27].

Among these models, the color-gradient model is widely used to simulate immiscible multiphase flow due to its high accuracy, strict mass conservation, and good numerical stability. In particular, it was applied to simulate an immiscible multiphase flow with large viscosity ratios [28,29].

In recent years, some scholars have conducted a series of simulation studies on various microscopic phenomena at the pore scale by the color-gradient model.

For instance, using a lattice Boltzmann color-gradient model, Huang et al. investigated the backflow in a pore doublet under forced imbibition conditions and the backflow for the forced imbibition in a dual-permeability pore network [30]. The results showed that the backflow can be ignored in the forced imbibition into a real porous medium. Gong et al. used the color-gradient model to investigate the spontaneous imbibition of capillary tubes with a variable diameter [31]. They found that the pore-throat aspect ratio and the pore-throat tortuosity can mainly affect the snap-off. Focusing on spontaneous imbibition in a single rectangular capillary, Li et al. presented a theoretical model. By comparing the simulated results with the theoretical solutions for various aspect ratios, they established the application condition of the quasi-3D color-gradient LBM [32]. By applying the color-gradient lattice Boltzmann model, Gu et al. investigated the dynamic behavior of droplets passing through a constricted square channel and various relevant factors, including the capillary number, initial drop size, viscosity ratio, and constriction length [33]. Based on the color-gradient lattice Boltzmann model, Fu et al. investigated the migration behaviors of droplets on a grooved surface and discussed the influence of surface roughness and the orientation of the surface topography [34]. Liu et al. used the color-gradient model to study the parallel immiscible two-phase flow in both solid free region and homogenized porous media region [35].

Although numerous simulation studies involving the color-gradient model have been conducted for the two-phase flow, it is obvious that researchers primarily focused on the imbibition, the flow types of droplets, and the two-phase flow in homogeneous or heterogeneous porous media. There is a lack of simulation research on the two-phase flow associated with blind-end that is widely distributed in porous media. Therefore, it is still unclear how much oil can be trapped in a single blind-end at the pore scale after the waterflooding process. Moreover, the impact of influencing factors related to fluid and blind-end structure on the oil phase in the blind-end needs to be discussed. In this paper, based on the LBM color-gradient model, we first analyzed the dynamic process of waterflooding for the oil in a blind-end and divided the entire process into stages. Furthermore, we investigated the effects of various influencing factors, including the viscosity ratio of oil to water, the flow velocity of water, the width of blind-end, the width of main channel, and the depth of blind-end, on the residual oil after the oil–water interface passed the blind-end. To the best of our knowledge, there is currently no literature reporting an investigation on the residual oil in a blind-end based on the color-gradient model.

2. Modeling and Method

2.1. Physical Problem Description

Figure 2 illustrates the schematic of the mechanism of residual oil formation in a blind-end. Generally, after the primary recovery, a large part of the reservoir has not been developed so that there is no fluid flow. Therefore, a blind-end with a micro-channel connected to it is filled with the oil phase at the initial stage, as shown in Figure 2a. Then, water is injected into the reservoir to displace the oil phase during waterflooding. Assuming the flow direction of water is left to right, after the two-phase interface just passes through the blind-end, a portion of the oil phase (residual oil) can be trapped in the blind-end, as shown in Figure 2b. Therefore, our research aims to investigate how much oil can

be trapped in the blind-end after the interface just passes through the blind-end under different influencing factors.

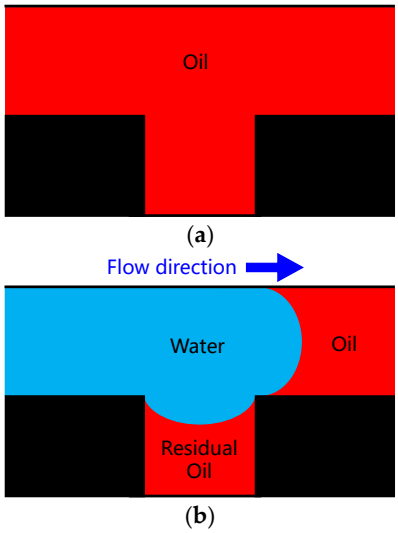


Figure 2. Schematic diagram of formation of residual oil in the blind-end. (**a**) Initial stage. (**b**) The two-phase interface passes through the blind-end.

2.2. Color-Gradient Model

In this study, we used a two-dimensional nine-velocity (D2Q9) color-gradient model that is written in C++. In this model, there are two types of fluid component, which are respectively called red fluid and blue fluid. The distribution functions of red fluid and blue fluid respectively are denoted as f_i^r and f_i^b, where the subscript i means the i-th direction of the discrete velocity. Then, the total distribution function can be expressed as $f_i = f_i^r + f_i^b$.

In each timestep, the red fluid distribution function and the blue fluid distribution function undergo a collision step and a streaming step, which can be expressed as [36]

$$f_i^r(\mathbf{x} + \mathbf{c}_i\delta_t, t + \delta_t) = f_i^r(\mathbf{x}, t) + \Omega_i^r[f_i^r(\mathbf{x}, t)] \tag{1}$$

$$f_i^b(\mathbf{x} + \mathbf{c}_i\delta_t, t + \delta_t) = f_i^b(\mathbf{x}, t) + \Omega_i^b\left[f_i^b(\mathbf{x}, t)\right] \tag{2}$$

where $\mathbf{x}$ is the position, t is the time, δ_t is the timestep, $\mathbf{c}_i$ is the lattice velocity in the i-th direction, Ω_i^r and Ω_i^b is the collision operator of red fluid and blue fluid.

The collision operators that consist of three parts can be expressed as [36]

$$\Omega_i^k = \left(\Omega_i^k\right)^{(3)}\left[\left(\Omega_i^k\right)^{(1)} + \left(\Omega_i^k\right)^{(2)}\right] \tag{3}$$

where k means red fluid or blue fluid, $\left(\Omega_i^k\right)^{(1)}$ is the Bhatnagar–Gross–Krook (BGK) collision operator, $\left(\Omega_i^k\right)^{(2)}$ is the perturbation operator which generates an interfacial tension, and $\left(\Omega_i^k\right)^{(3)}$ is the recoloring operator which contributes to maintaining the phase interface.

The $\left(\Omega_i^k\right)^{(1)}$ can be expressed as

$$\left(\Omega_i^k\right)^{(1)} = -\omega\left[f_i^k - f_i^{k(eq)}\right] \tag{4}$$

where ω is the relaxation parameter [36], $f_i^{k(eq)}$ is the equilibrium distribution.

The equilibrium distribution can be expressed as [37]

$$f_i^{k(eq)} = \rho^k W_i \left(1 + \frac{3}{c^2}\mathbf{c}_i \cdot \mathbf{u} + \frac{9}{2c^2}(\mathbf{c}_i \cdot \mathbf{u})^2 - \frac{3}{2c^2}(\mathbf{u})^2\right) \tag{5}$$

where ρ^k is the density of red fluid or blue fluid, and $\mathbf{u}$ is the velocity of fluid mixture.

The weight factor W_i can be expressed as

$$W_i = \begin{cases} 4/9, i = 0 \\ 1/9, i = 1 \sim 4 \\ 1/36, i = 5 \sim 8 \end{cases} \tag{6}$$

The lattice velocity $\mathbf{c}_i$ can be expressed as

$$\mathbf{c}_i = \begin{cases} (0,0), i = 0 \\ (\pm 1, 0)c, (0, \pm 1)c, i = 1 \sim 4 \\ (\pm 1, \pm 1)c, i = 5 \sim 8 \end{cases} \tag{7}$$

The macroscopic densities can be expressed as

$$\rho^k = \sum_i f_i^{k(eq)} \tag{8}$$

The macroscopic velocity can be expressed as

$$\rho \mathbf{u} = \sum_i \sum_k \mathbf{c}_i f_i^{k(eq)} \tag{9}$$

where ρ is the total density which can be expressed as $\rho = \rho^r + \rho^b$.

The macroscopic pressure can be expressed as

$$p = c_s^2 \tag{10}$$

The speed of sound c_s can be expressed as

$$c_s = \frac{c}{\sqrt{3}} \tag{11}$$

where $c = \Delta x / \Delta t = 1$ is the ratio of lattice spacing and time step.

The $\left(\Omega_i^k\right)^{(2)}$ can be expressed as [38]

$$\left(\Omega_i^k\right)^{(2)} = A^k W_i \left(1 - \frac{\omega}{2}\right)[3(\mathbf{c}_i - \mathbf{u}) + 9(\mathbf{c}_i \cdot \mathbf{u})\mathbf{c}_i] \cdot \mathbf{F} \tag{12}$$

where A^k is the fraction of interfacial tension contributed by the fluid k and satisfies $\sum_k A_k = 1$.

The capillary force $\mathbf{F}$ can be expressed as [36]

$$\mathbf{F} = -\frac{1}{2}\sigma K \nabla \rho^N \tag{13}$$

where σ is the interfacial tension coefficient, ρ^N is the phase field function responsible for differentiating different fluids, K is the local curvature of the interface.

The phase field function ρ^N can be expressed as

$$\rho^N = \frac{\rho^r - \rho^b}{\rho^r + \rho^b} \tag{14}$$

The local curvature of the interface K can be expressed as

$$K = -\nabla_S \cdot \mathbf{n} \tag{15}$$

where $\nabla_S = (\mathbf{I} - \mathbf{nn}) \cdot \nabla$ is the surface gradient operator, $\mathbf{n}$ is the outward-pointing unit normal vector of interface.

$\mathbf{n}$ can be expressed as

$$\mathbf{n} = -\frac{\nabla \rho^N}{|\nabla \rho^N|} \tag{16}$$

The macroscopic velocity can be redefined as

$$\rho \mathbf{u} = \sum_i \sum_k \mathbf{c}_i f_i^k + 0.5\mathbf{F} \tag{17}$$

To promote phase segregation and maintain a reasonable interface, the segregation operator of Latva-Kokko and Rothman [39] is expressed as

$$(\Omega_i^r)^{(3)}(f_i') = \frac{\rho^r}{\rho} f_i' + \beta W_i \frac{\rho^r \rho^b}{\rho} \cos(\varphi_i) |\mathbf{c}_i| \tag{18}$$

$$\left(\Omega_i^b\right)^{(3)}(f_i') = \frac{\rho^b}{\rho} f_i' - \beta W_i \frac{\rho^r \rho^b}{\rho} \cos(\varphi_i) |\mathbf{c}_i| \tag{19}$$

where f_i' is the post-perturbation value of the total distribution function; φ_i is the angle between the color gradient $\nabla \rho^N$ and $\mathbf{c}_i$; and β is a parameter associated with the interface thickness and taken as 0.7.

Using the Chapman–Enskog multiscale analysis, Equations (1) and (2) can be reduced to the Navier–Stokes equation [40]

$$\frac{\partial \rho}{\partial t} + \nabla \cdot (\rho \mathbf{u}) = 0 \tag{20}$$

2.3. Characterization of Typical Blind-End

The schematic diagram of the simulation domain is shown in Figure 3, which mainly includes a main channel, an inlet, an outlet, and a blind-end. The black line represents the solid wall. The black area represents the solid area. The red line represents the inlet. The yellow line represents the outlet. The blue area represents the main channel, and the green area represents the blind-end. The water is continuously injected at the constant flow velocity from the left inlet, while a fully developed boundary is imposed at the right outlet.

It should be noted that the current study employs a two-dimensional (2D) model that simplifies the spatial information of the realistic microstructure of reservoir. In addition, while the 2D model allows for a detailed investigation with high computational efficiency, it probably is not able to fully present complex three-dimensional (3D) flow behaviors with gravity. Therefore, an extension of this work is to develop a 3D model to address these limitations and achieve better spatial fidelity.

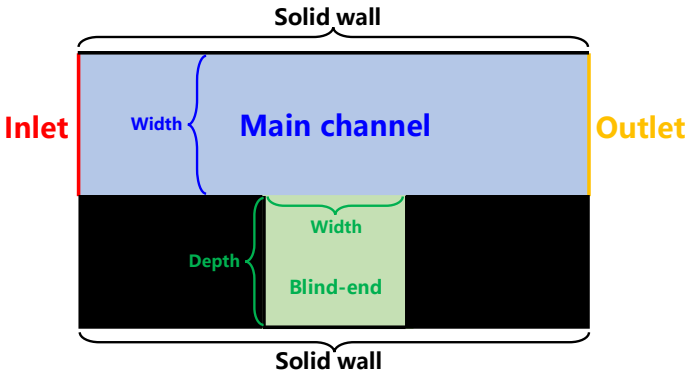


Figure 3. Schematic diagram of simulation domain.

3. Validation

3.1. Young–Laplace Equation

According to Young–Laplace equation, the relationship of the pressure difference between inside and outside of a droplet and the radius of the droplet is expressed as

$$\Delta p = \frac{\sigma}{R} \tag{21}$$

where σ is the interfacial tension.

To verify the accuracy of the model, we defined a simulation domain (500 lu $\times$ 500 lu) with the periodic boundary condition. The simulation domain is filled with blue fluid and then droplets (red fluid) with different radii were placed in the middle of this domain. The relationship between Δp and $1/R$ is shown in Figure 4. As shown in Figure 4, the Δp follows a linear relationship with the $1/R$ and the slope is approximately consistent with the interfacial tension 0.1. This proves that the model conforms to Young–Laplace equation.

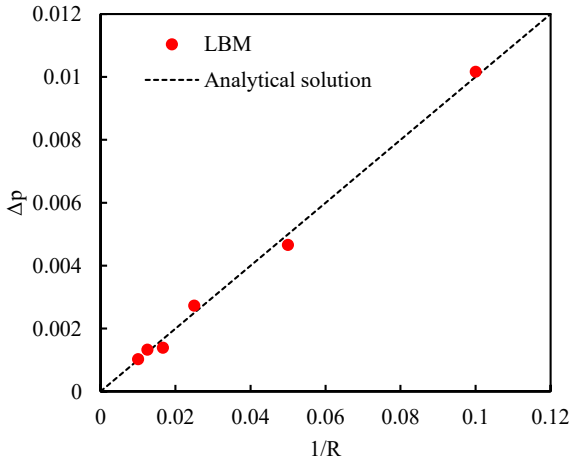


Figure 4. Validation of Young–Laplace's law.

3.2. Wettability

In the color-gradient model, the wettability is achieved through ρ^N. The ρ^N is in the range $-1 \leq x \leq 1$. The value of ρ^N corresponds to the contact angle. To verify the accuracy of the model, we defined a simulation domain (200 lu $\times$ 100 lu). The periodic boundary is imposed at both left side and right side of the domain. The top and bottom of the domain are solid wall. The simulation domain is filled with blue fluid and then a portion of red fluid is placed on the bottom solid wall. The relationship between the ρ^N and the contact angle θ is shown in Figure 5. As shown in Figure 5, it can be seen that there is a linear

relationship between the contact angle θ and the ρ^N. For subsequent simulation cases, the value of ρ^N is -0.4, which means the wettability is oil-wet.

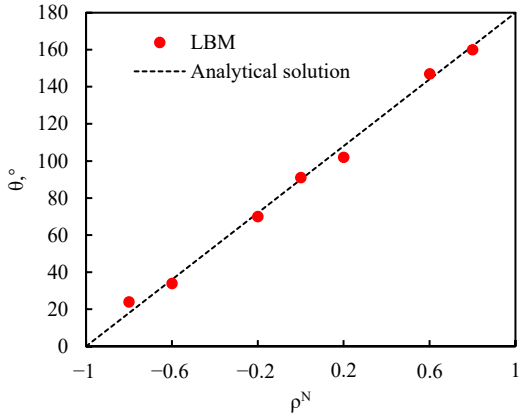


Figure 5. Validation of wettability.

3.3. Simulation Scale

Simulation cases were performed at varying scales, ranging from 125 lu × 50 lu to 1000 lu × 400 lu. All simulation cases lasted for 200,000 timesteps. the physical property of both fluids is $\rho^r = \rho^b = 1$. The flow velocity of water is 0.01 lu/ts. In our study, the oil saturation was obtained by using the image analysis software Fiji Image J (Version 1.54j 12 June 2024). Figure 6 demonstrates that the variation in oil saturation of the entire simulation domain with simulation scale at the last timestep. It can be seen that the influence of simulation scale was obvious before 500 lu × 200 lu. The error between 500 lu × 200 lu and 1000 lu × 400 lu was only 0.31%, rendering it negligible.

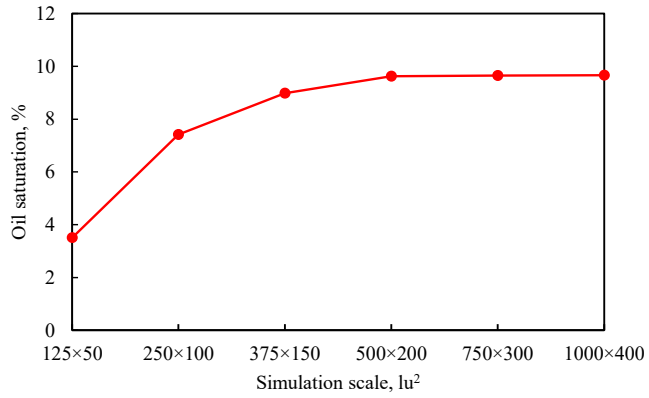


Figure 6. Variation in oil saturation of entire simulation domain with simulation scale.

3.4. Numerical Stability

We selected a simulation case to check the numerical stability. The simulation domain size is 500 lu × 200 lu. The physical property of both fluids is $\rho^r = \rho^b = 1$. The flow velocity of water is 0.01 lu/ts. The width and depth of blind-end is respectively 100 lu and 100 lu. The width of main channel is 100 lu. The simulation lasted for 200,000 timesteps. Figure 7 demonstrates that the variation in oil saturation of entire simulation domain with timesteps. It can be seen that the oil saturation of entire simulation domain remains constant as the timestep increases when the timestep exceeds 80,000. This indicates that the oil saturation of entire simulation domain can achieve a stable state.

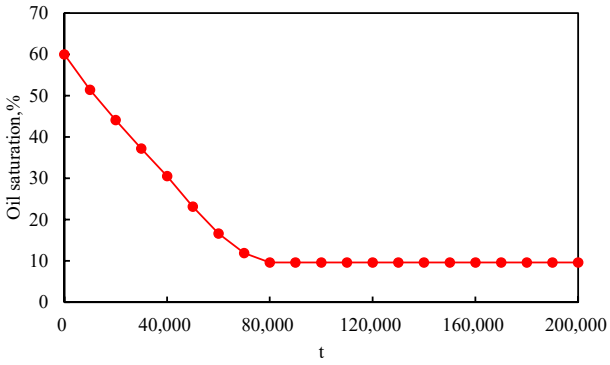


Figure 7. Variation in oil saturation of entire simulation domain with timestep.

4. Results and Discussion

In this section, we first described the dynamic process of waterflooding for the oil in blind-end, and then discussed the impact of different factors on the oil phase in blind-end after the interface of the two phases passed through the blind-end, including the velocity of water, the viscosity ratio of oil to water, the width of the blind-end, the width of the main channel, and the depth of the blind-end.

4.1. Dynamic Displacement Process of Water for Oil in Blind-End

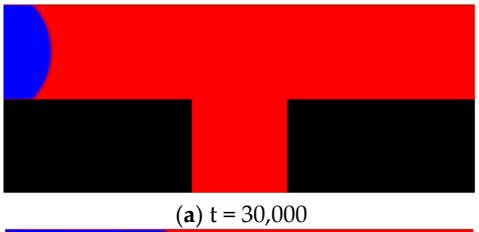
We selected a simulation case to describe the dynamic displacement process. The simulation domain size is 500 lu × 200 lu. The viscosity ratio of oil to water is 1. The flow velocity of water is 0.002 lu/ts. The width and depth of the blind-end is, respectively, 100 lu and 100 lu. The width of the main channel is 100 lu.

Figures 8–11 demonstrates the process based on abovementioned parameters. The water is blue and the oil is red. The solid area is black. The initial state is shown in Figure 8, the main channel and the blind-end are initially saturated by the oil.

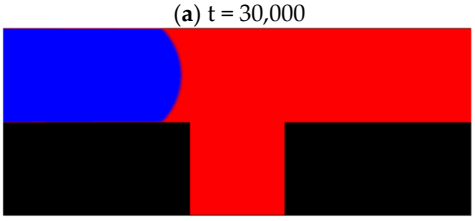


t = 0

Figure 8. Initial state of displacement process.

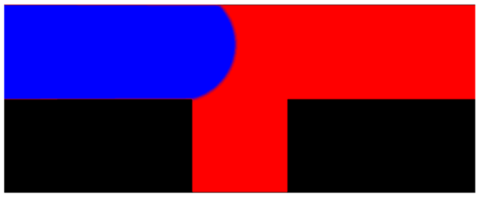


(**a**) t = 30,000

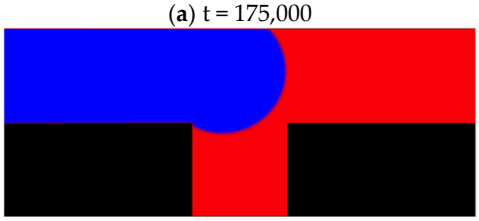


(**b**) t = 135,000

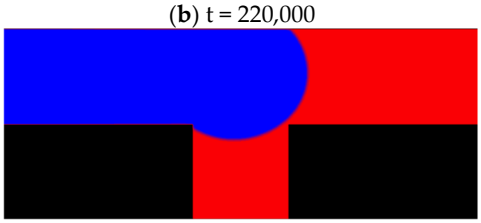
Figure 9. Movement of two-phase interface.



(**a**) t = 175,000

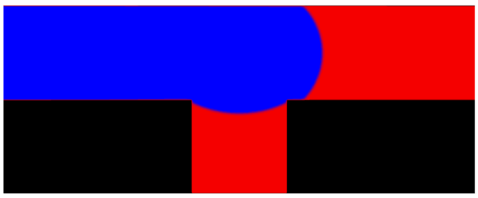


(**b**) t = 220,000



(**c**) t = 240,000

Figure 10. Invasion of water.



t = 250,000

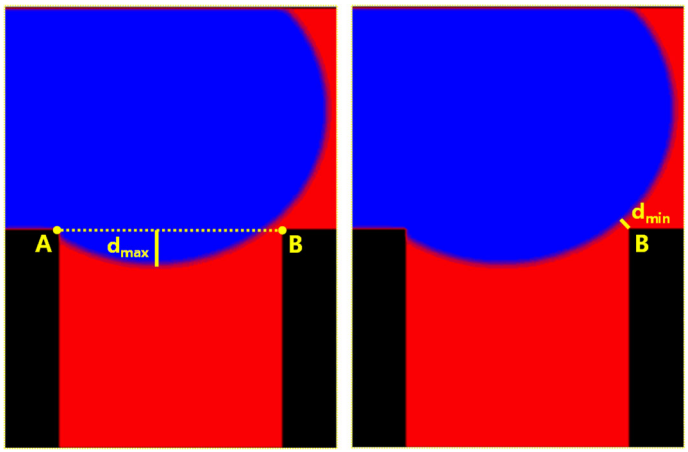
Figure 11. Retention of oil in blind-end.

This dynamic process can be mainly divided into three stages. First, the movement of the two-phase interface. As shown in Figure 9a,b, driven by the water, the two-phase interface first moves forward along the main channel.

Second, the invasion of water. When the two-phase interface moves to the blind-end, the two-phase interface expands gradually. Furthermore, a portion of the area inside the blind-end is occupied by the water, as shown in Figure 10a,b. As the displacement time increases, the two-phase interface further moves forward and becomes longer, as shown in Figure 10c. Meanwhile, the water occupies more of the interior area of the blind-end.

Third, the retention of oil in the blind-end. It can be seen from Figure 11 that a portion of oil phase (residual oil) remains in the blind-end after the two-phase interface just passes through the blind-end.

We defined the residual oil saturation of blind-end as the ratio of the area of residual oil in a blind-end to the total area of a blind-end (depth of blind-end $\times$ width of blind-end) after the two-phase interface just passes through the blind-end. In the following content, we discussed the variation in residual oil saturation of the blind-end with influencing factors. To enable a more quantitative mechanistic analysis, we defined two parameters, d_{min} and d_{max}, based on Figure 10c, as shown in Figure 12. It can be seen that the d_{max} that is perpendicular to the dotted line, AB is the longest distance between dotted line, AB and the internal two-phase interface in the blind-end. It can be seen that the d_{min} is the shortest distance between the two-phase interface and the solid endpoint B.



(**a**) d_{max} (**b**) d_{min}

Figure 12. Schematic diagram of d_{max} and d_{min}.

4.2. Effect of Flow Velocity of Water

During the waterflooding process, water is injected from the injection well and then flows to the production well. Between the injection well and the production well, the flow velocity of water varies in different regions. Generally, the flow velocity of water in the region near the injection well or the production well is higher, while the flow velocity of water in the region far away from the production well and the injection well (the middle region between the two types of well) is lower. Therefore, the flow velocity of water is an important influencing factor.

We simulated seven cases to investigate the effect of flow velocity of water on the residual oil in the blind-end, ranging from 0.0001 to 0.075 lu/ts. For these seven cases, the physical property of both fluids is $\rho^r = \rho^b = 1$. The width and depth of blind-end is respectively 100 lu and 100 lu. The width of main channel is 100 lu.

Figure 13 demonstrates the variation in residual oil saturation of the blind-end with the flow velocity of water. As shown in Figure 13, as the velocity of water increases from 0.0001 to 0.075 lu/ts, the residual oil saturation of blind-end increases from 83.9% to 94.6%. This indicates that the higher velocity of water can result in more oil retention in the blind-end. Additionally, it can be seen that when the velocity of water is relatively low (0.0001–0.005 lu/ts), the residual oil saturation increases significantly with the increase in velocity of water. It also can be seen that when the velocity of water is relatively high (0.005–0.075 lu/ts), the increase in residual oil saturation is slower with the increase in velocity of water.

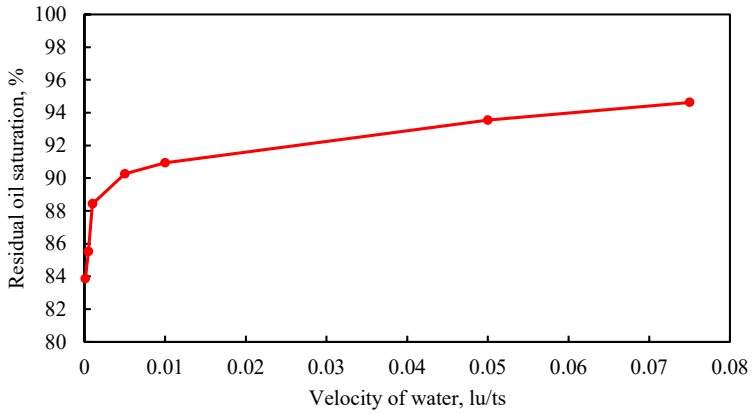
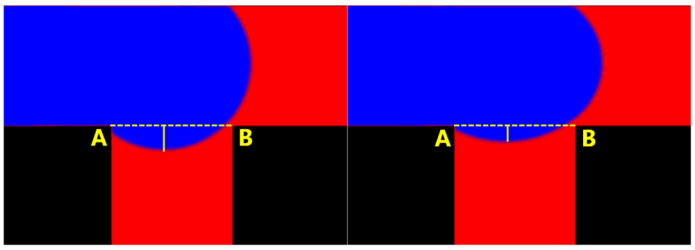


Figure 13. Variation in residual oil saturation with flow velocity of water.

Figure 14 compared the state of two-phase interface of two cases (0.0001 lu/ts and 0.01 lu/ts) when the d_{min} of both cases is about 6 lu. The d_{max} of both cases (the vertical line) is respectively 22 lu (0.0001 lu/ts) and 13 lu (0.01 lu/ts). It can be seen that when the velocity of water is lower (0.0001 lu/ts), the water phase can effectively invade the inside of the blind-end and occupy more space. This is mainly because the two-phase interface has ample time to expand further. When the velocity of water is higher (0.01 lu/ts), the water phase can push the two-phase interface to rapidly move forward, which reduces the expansion of the two-phase interface, resulting in that the water phase is unable to effectively invade the inner space of the blind-end. Therefore, there is more oil trapped in the blind-end after the two-phase interface just passes through the blind-end.



(**a**) 0.0001 lu/ts (**b**) 0.01 lu/ts

Figure 14. Comparison of d_{max} of two cases (velocity 0.0001 lu/ts and velocity 0.01 lu/ts).

4.3. Effect of Viscosity Ratio of Oil to Water

The viscosity of crude oil in the underground reservoir usually varies significantly. In some reservoirs, the viscosity of crude oil is nearly the same as that of water, while in others, it can be thousands of times higher than the viscosity of water.

We simulated 8 cases to investigate the effect of viscosity ratio of oil to water on the residual oil in the blind-end, ranging from 1 to 100. For these 8 cases, the physical property of both fluids is $\rho^r = \rho^b = 1$. The flow velocity of water is 0.001 lu/ts. The width and depth of blind-end is respectively 100 lu and 100 lu. The width of main channel is 100 lu.

Figure 15 demonstrates the variation in residual oil saturation of blind-end with the viscosity ratio of oil to water. As shown in Figure 15, as the viscosity ratio of oil to water increases from 1 to 100, the residual oil saturation of the blind-end increases from 88.4% to 93.7%. Additionally, it can be seen that when the viscosity ratio of oil to water is relatively low (1–25), the residual oil saturation increases slowly. It also can be seen that when the viscosity ratio of oil to water is relatively high (25–100), the residual oil saturation gradually stabilizes with the increase in the viscosity ratio.

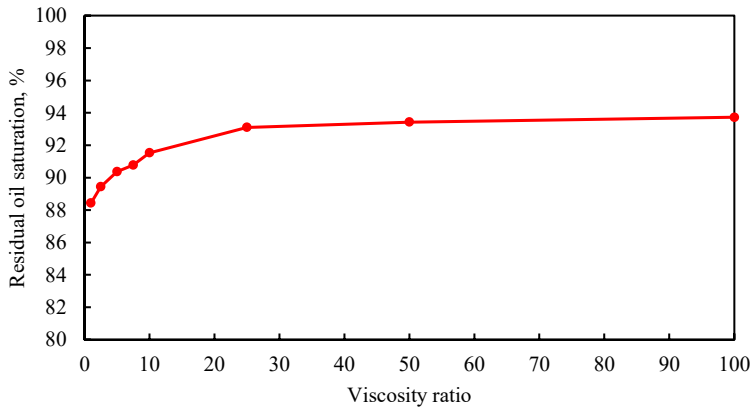


Figure 15. Variation in residual oil saturation with viscosity ratio.

This is mainly because both oil and water are easy to flow when the viscosity ratio of oil to water is low. Therefore, the two-phase interface can sufficiently expand when

the two-phase interface moves to the blind-end so that the water phase can occupy more internal space of the blind-end. When the viscosity ratio of oil to water is high, the flow ability of the oil phase decreases. Then, the two-phase interface is difficult to sufficiently expand when it reaches the blind-end. Therefore, there is more oil trapped in the blind-end after the two-phase interface just passes through the blind-end.

4.4. Effect of Width of Blind-End

We simulated eight cases to investigate the effect of the width of blind-end on the residual oil in the blind-end, ranging from 50 to 225 lu. For these eight cases, the physical property of both fluids is $\rho^r = \rho^b = 1$. The flow velocity of water is 0.001 lu/ts. The depth of blind-end and the width of main channel is respectively 100 lu and 100 lu.

Figure 16 demonstrates the variation in residual oil saturation of blind-end with the width of the blind-end. As shown in Figure 16, as the width of the blind-end increases from 50 to 225 lu, the residual oil saturation of the blind-end decreases from 97.3% to 29.6%. This indicates that the wider blind-end can result in the lower oil retention in the blind-end.

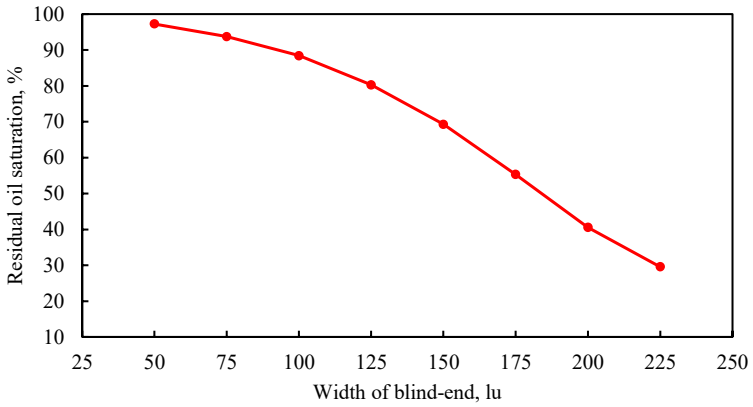
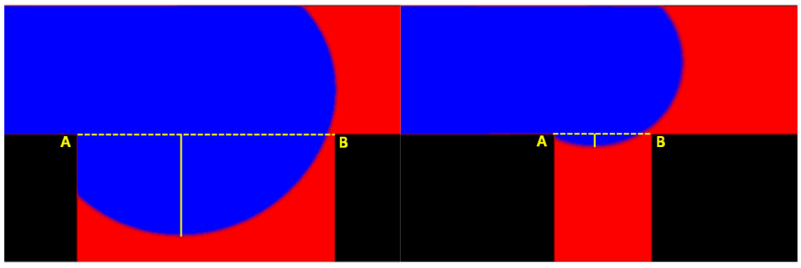


Figure 16. Variation in residual oil saturation with width of blind-end.

Figure 17 compares the state of the two-phase interface in the two cases (blind-end width 200 lu and blind-end width 75 lu) when the d_{min} of both cases is about 6 lu. The d_{max} of both cases (the vertical line) is respectively 79 lu (blind-end width 200 lu) and 10 lu (blind-end width 75 lu). This is mainly because the blind-end with higher width can result in the lower capillary force in the vertical direction and then promote the expansion of the two-phase interface towards the interior of the blind-end. For the blind-end with lower width, due to the higher capillary force in the vertical direction, the interface is pushed forward by the water phase and then passes through the blind-end before the two-phase interface can sufficiently expand, leading to more oil trapped in the blind-end.



(**a**) 200 lu (**b**) 75 lu

Figure 17. Comparison of d_{max} of two cases (blind-end width 200 lu and blind-end width 75 lu).

4.5. Effect of Width of Main Channel

We simulated 10 cases to investigate the effect of the width of main channel on the residual oil in the blind-end, ranging from 20 to 200 lu. For these 10 cases, the physical

property of both fluids is $\rho^r = \rho^b = 1$. The flow velocity of water is 0.001 lu/ts. The width and depth of blind-end are, respectively, 100 lu and 100 lu.

Figure 18 demonstrates the variation in residual oil saturation of blind-end with the width of the main channel. As shown in Figure 18, as the width of the main channel increases from 20 to 200 lu, the residual oil saturation of the blind-end increases from 66.1% to 96.8%.

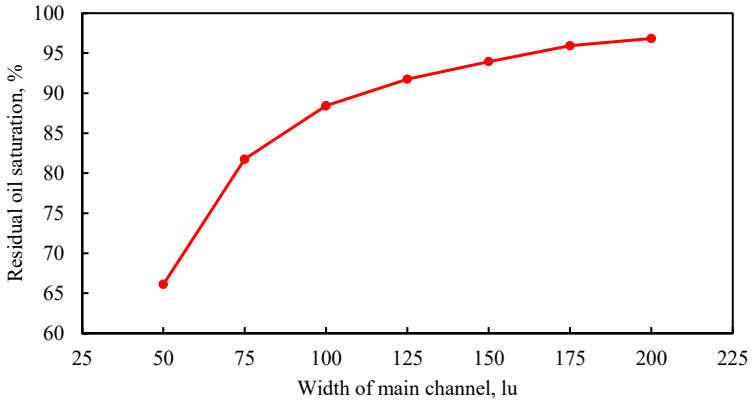
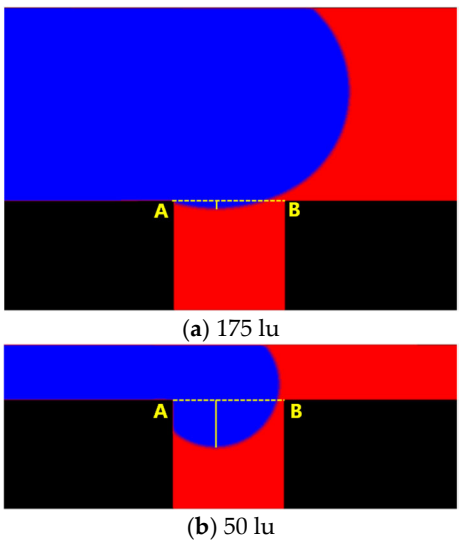


Figure 18. Variation in residual oil saturation with width of main channel.

Figure 19 compares the state of the two-phase interface of the two cases (main channel width 175 lu and main channel width 50 lu) when the d_{min} of both cases is about 6 lu. The d_{max} of both cases (the vertical line) is respectively 42 lu (main channel width 175 lu) and 8 lu (main channel width 50 lu). This is mainly because the main channel with lower width can result in higher capillary force in the horizontal direction and then promote the expansion of the two-phase interface towards the interior of the blind-end. For the main channel with higher width, due to the lower capillary force in the horizontal direction, the interface has a stronger tendency to move forward due to the push by the water phase and then passes through the blind-end before the two-phase interface sufficiently expands, leading to more oil trapped in the blind-end.



(**a**) 175 lu

(**b**) 50 lu

Figure 19. Comparison of d_{max} of two cases (main channel width 175 lu and main channel width 50 lu).

4.6. Effect of Depth of Blind-End

We simulated 10 cases to investigate the effect of the depth of the blind-end on the residual oil in the blind-end, ranging from 20 to 200 lu. For these 10 cases, the physical

property of both fluids is $\rho^r = \rho^b = 1$. The flow velocity of water is 0.001 lu/ts. The width of the blind-end is 100 lu. The width of the main channel is 100 lu.

Figure 20 demonstrates the variation in residual oil saturation of blind-end with the depth of the blind-end. As shown in Figure 20, as the depth of the blind-end increases from 20 to 200 lu, the residual oil saturation of the blind-end increases from 66.1% to 96.8%.

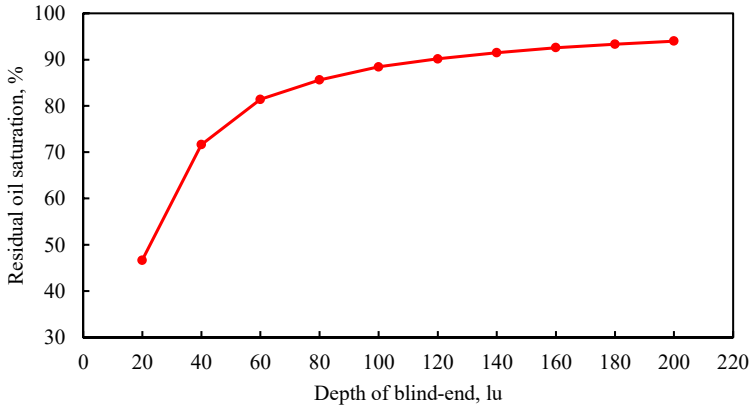
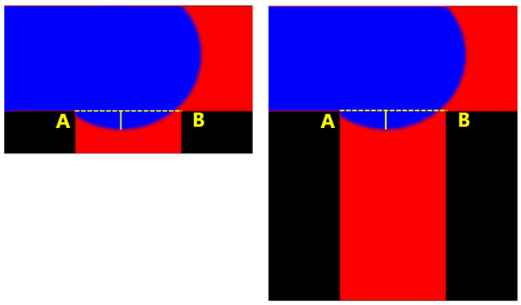


Figure 20. Variation in residual oil saturation with depth of blind-end.

Figure 21 compares the state of the two-phase interface of the two cases (blind-end depth 40 lu and blind-end depth 180 lu) when the d_{min} of both cases is about 6 lu. The d_{max} of both (the vertical line) cases is 18 lu. This is mainly because once the two-phase interface moves to the blind-end, the capillary force is not affected by the variation in blind-end depth due to the constant widths of both the blind-end and the main channel. Therefore, the same extent of expansion of the two-phase interface leads to the same extent invasion of the water phase. Because the deep blind-end contains more oil than the shallow blind-end, the residual oil saturation of the blind-end increases with the increase in the depth of the blind-end.



(**a**) 40 lu (**b**) 180 lu

Figure 21. Comparison of d_{max} of two cases (blind-end depth 40 lu and blind-end depth 180 lu).

5. Conclusions

In this study, we used the LBM color-gradient model to study the dynamic displacement process of water for oil in a blind-end and analyzed the residual oil after the oil–water interface passed the blind-end under different factors.

The LBM simulation results are summarized as follows. When a blind-end is saturated with oil, the dynamic displacement process of water for oil in a blind-end can be divided into three stages, including the movement of the two-phase interface, the invasion of water, and the retention of oil in the blind-end. After the two-phase interface passes through the blind-end, the residual oil saturation of the blind-end increases with the increase in the velocity of water, the viscosity ratio of oil to water, the width of the main channel, and the

depth of the blind-end. Meanwhile, the residual oil saturation of the blind-end decreases with the increase in the width of the blind-end.

Based on the findings of this study, the following research directions are proposed:

(1) Expanding the model from the current two-dimensional (2D) to a full three-dimensional (3D) model allows for the analysis of various flow phenomena in a more realistic microstructure, such as the blind-end structure derived from CT scans.
(2) Extending the simulation from the single geometry to the networks interconnected with the pore-throat can further validate the model's robustness and investigate oil retention in more realistic porous media.
(3) The polymer, such as the hydrolyzed polyacrylamide, is a type of chemical agent commonly used in oilfield to enhance oil recovery. It is not clear whether the viscoelasticity of polymer has an effect on the retention of oil in the blind-end.
(4) The surfactant, especially various anionic surfactants that are commonly used in oilfields, can alter the wettability of rocks. Therefore, it is worthwhile to investigate the effect of wettability change on the retention of oil in the blind-end in the presence of the surfactant.

Author Contributions: Conceptualization, H.W.; Writing—original draft, H.W.; Review and editing, Y.W., Q.L., G.W., and L.L. All authors have read and agreed to the published version of the manuscript.

Funding: This research was funded by the National Natural Science Foundation of China (grant number U25B6006), the postdoctoral scientific research project of Shengli oilfield of Sinopec (grant number YKB2524), the Shandong postdoctoral science foundation (grant number SDZZ-ZR-202501212), the scientific research project of Shengli oilfield of Sinopec (grant number YKY2503) and the scientific research project of Sinopec (grant number P25120).

Institutional Review Board Statement: Not applicable.

Informed Consent Statement: Not applicable.

Data Availability Statement: The original contributions presented in the study are included in the article, further inquiries can be directed to the corresponding author.

Conflicts of Interest: The authors declare no conflicts of interest. The authors were employed by the Sinopec. The Sinopec had no role in the design of the study; in the collection, analyses, or interpretation of data; in the writing of the manuscript, or in the decision to publish the results.

Nomenclature

f_i^r	distribution function of red fluid
f_i^b	distribution function of blue fluid
f_i	total distribution function
δ_t	timestep
$\mathbf{c}_i$	lattice velocity
$\left(\Omega_i^k\right)^{(1)}$	BGK collision operator
$\left(\Omega_i^k\right)^{(2)}$	perturbation operator
$\left(\Omega_i^k\right)^{(3)}$	recoloring operator
ω	relaxation parameter
$f_i^{k(eq)}$	equilibrium distribution
W_i	weight factor
ρ^k	fluid density
$\mathbf{u}$	fluid velocity
p	macroscopic pressure

c_s	speed of sound
c	ratio of lattice spacing and time step
A^k	fraction of interfacial tension contributed by fluid
$\mathbf{F}$	capillary force
σ_c	interfacial tension coefficient
K	local curvature of interface
∇_S	surface gradient operator
$\mathbf{n}$	outward-pointing unit normal vector of interface
f_i^*	post-perturbation value of total distribution function
ρ^N	phase field function
Δp	pressure difference
θ	contact angle
R	droplet radius
σ	interfacial tension

References

1. Dieterle, M.; Schwab, E. Raw Material Change in the Chemical Industry. *Top. Catal.* **2016**, *59*, 817–822. [CrossRef]
2. Anwer, E.; Rizk, A.S.; Muaz, A.; Abdelfadil, M. Evaluation of Waterflooding Project Technical Viability in a Clastic Sandstone Reservoir: A Case Study in Western Desert, Egypt. In Proceedings of the Mediterranean Offshore Conference, Alexandria, Egypt, 20–22 October 2024.
3. Tavakkoli, O.; Kamyab, H.; Shariati, M.; Mohamed, A.M.; Junin, R. Effect of Nanoparticles on the Performance of Polymer/Surfactant Flooding for Enhanced Oil Recovery: A Review. *Fuel* **2022**, *312*, 122867. [CrossRef]
4. Kumar, N.; Sampaio, M.A.; Ojha, K.; Hoteit, H.; Mandal, A. Fundamental Aspects, Mechanisms and Emerging Possibilities of CO_2 Miscible Flooding in Enhanced Oil Recovery: A Review. *Fuel* **2022**, *330*, 125633. [CrossRef]
5. Zheng, S.; Wang, X.; Chen, J.; Gu, H.; Wu, W. Multiphase Flow Simulation of Fractured Karst Oil Reservoirs Applying Three-Dimensional Network Models. *Phys. Fluids* **2024**, *36*, 076610. [CrossRef]
6. Kazem, M.; Hussein, M.; Ojha, K.; Adnan, M.; Alfarge, D.; Mansour, I. The Performance of Streamline Simulation Technique to Mimic the Waterflooding Management Process in Oil Reservoirs. *Fuel* **2023**, *348*, 128556. [CrossRef]
7. Ambekar, A.S.; Mattey, P.; Buwa, V.V. Pore-resolved Two-phase Flow in a Pseudo-3D Porous Medium: Measurements and Volume-of-fluid Simulations. *Chem. Eng. Sci.* **2021**, *230*, 116128. [CrossRef]
8. Yue, M.; Zhu, W.; Han, H.; Song, H.; Long, Y.; Lou, Y. Experimental Research on Remaining Oil Distribution and Recovery Performances after Nano-micron Polymer Particles Injection by Direct Visualization. *Fuel* **2018**, *212*, 506–514. [CrossRef]
9. Lv, Q.; Zhou, T.; Zhang, X.; Zuo, B.; Dong, Z.; Zhang, J. Enhanced Oil Recovery Using Aqueous CO_2 Foam Stabilized by Particulate Matter from Coal Combustion. *Energy Fuels* **2020**, *34*, 2880–2892. [CrossRef]
10. Mohammadi, M.; Mahani, H. Direct Insights into the Pore-scale Mechanism of Low-Salinity Waterflooding in Carbonates Using a Novel Calcite Microfluidic Chip. *Fuel* **2020**, *260*, 116374. [CrossRef]
11. Du, Y.; Xu, K.; Mejia, L.; Zhu, P.; Balhoff, M.T. Microfluidic Investigation of Lowsalinity Effects during Oil Recovery: A No-clay and Time-dependent Mechanism. *SPE J.* **2019**, *24*, 2841–2858. [CrossRef]
12. Wang, D.; Cheng, J.; Yang, Q.; Gong, W.; Li, Q. Viscous-elastic Polymer Can Increase Microscale Displacement Efficiency in Cores. In Proceedings of the SPE Annual Technical Conference and Exhibition, Dallas, TX, USA, 1–4 October 2000.
13. Wang, D.; Liu, C.; Wu, W.; Wang, G. Development of an Ultra-low Interfacial Tension Surfactant in a System with No-alkali for Chemical Flooding. In Proceedings of the SPE Symposium on Improved Oil Recovery, Tulsa, OK, USA, 20–23 April 2008.
14. Yekeen, N.; Padmanabhan, E.; Syed, A.H.; Sevoo, T.; Kanesen, K. Synergistic Influence of Nanoparticles and Surfactants on Interfacial Tension Reduction, Wettability Alteration and Stabilization of Oil-in-water Emulsion. *J. Pet. Sci. Eng.* **2020**, *186*, 106779. [CrossRef]
15. Li, K.; Jing, X.; Qu, D.; Pu, W.; Wei, B. Pore-level Investigations on the Oil Displacement Mechanisms of a Viscoelastic Surfactant in Porous Media. *J. Pet. Sci. Eng.* **2019**, *173*, 748–757. [CrossRef]
16. Liu, W.; Luo, L.; Liao, G.; Zuo, L.; Wei, Y.; Jiang, W. Experimental Study on the Mechanism of Enhancing Oil Recovery by Polymer-surfactant Binary Flooding. *Pet. Explor. Dev.* **2017**, *44*, 636–643. [CrossRef]
17. Giordano, M.G.; Jacob, J.; Fusco, P.; Tangaro, S.; Malcangio, D. Vertical Dense Jets in Crossflows: A Preliminary Study with Lattice Boltzmann Methods. *Fluids* **2025**, *10*, 159. [CrossRef]
18. Peng, F.; Zhang, S.; Wu, K. Study on Spontaneous Capillary Imbibition in Irregular Geometries Using the Lattice Boltzmann Approach. *Processes* **2025**, *13*, 3527. [CrossRef]

19. Quintero-Castañeda, C.Y.; Sierra-Carrillo, M.M.; Villegas-Andrade, A.I.; Burgos-Vergara, J. Numerical Simulation of First-Order Surface Reaction in Open Cavity Using Lattice Boltzmann Method. *Fluids* **2025**, *10*, 7. [CrossRef]
20. Guo, W.; Zhao, J.; Wang, G.; Fang, M.; Zhu, K. Effect of Pore-Scale Anisotropic and Heterogeneous Structure on Rarefied Gas Flow in Three-Dimensional Porous Media. *Fluids* **2025**, *10*, 175. [CrossRef]
21. Wang, N.; Ni, W.; Liu, H. Geometrical Wetting Boundary Condition for Complex Geometries in Lattice Boltzmann Color-gradient Model. *Phys. Fluids* **2024**, *36*, 012109. [CrossRef]
22. Wang, N.; Kuang, T.; Liu, Y.; Yin, Z.; Liu, H. Wetting Boundary Condition for Three-dimensional Curved Geometries in Lattice Boltzmann Color-gradient Model. *Phys. Fluids* **2024**, *36*, 032133. [CrossRef]
23. Wang, W.; Xie, Q.; Wang, H.; Su, Y.; Gomari, S. Pseudopotential-based Multiple-relaxation-time Lattice Boltzmann Model for Multicomponent and Multiphase Slip Flow. *Adv. Geo-Energy Res.* **2023**, *9*, 106–116. [CrossRef]
24. Swift, M.R.; Orlandini, E.; Osborn, W.R.; Yeomans, J.M. Lattice Boltzmann Simulations of Liquid-gas and Binary Fluid Systems. *Phys. Rev. E* **1996**, *54*, 5041. [CrossRef]
25. Bouchard, R.; Younes, N.; Millet, O.; Wautier, A. Parameter Optimization of Phase-field-based LBM Model for Calculating Capillary Forces. *Comput. Geotech.* **2024**, *172*, 106391. [CrossRef]
26. Wang, H.; Cai, J.; Su, Y.; Jin, Z.; Wang, W.; Li, G. Imbibition Behaviors in Shale Nanoporous Media from Pore-scale Perspectives. *Capillarity* **2023**, *9*, 32–44. [CrossRef]
27. Yin, Y.; Wang, H.; Zuo, H.; Zhang, T. An Upscaling Framework for Predicting Gas Multiscale Transport Behavior in Shale Matrix-Microfracture Systems Considering Microscopic Transport Mechanisms. *Phys. Fluids* **2025**, *37*, 022002. [CrossRef]
28. Zahid, F.; Cunningham, J.A. Review of the Color Gradient Lattice Boltzmann Method for Simulating Multi-phase Flow in Porous Media: Viscosity, Gradient Calculation, and Fluid Acceleration. *Fluids* **2025**, *10*, 128. [CrossRef]
29. Huang, H.; Wang, L.; Lu, X. Evaluation of Three Lattice Boltzmann Models for Multiphase Flows in Porous Media. *Comput. Math. Appl.* **2011**, *61*, 3606–3617. [CrossRef]
30. Huang, Y.; Wang, N.; Liu, H.; Kuang, T.; Yin, Z. Does Backflow Occur in Forced Imbibition into a Dual-permeability Pore Network? *Int. J. Multiph. Flow* **2024**, *174*, 104782. [CrossRef]
31. Gong, R.; Wang, X.; Li, L.; Li, K.; An, R.; Xian, C. Lattice Boltzmann Modeling of Spontaneous Imbibition in Variable-diameter Capillaries. *Energies* **2022**, *15*, 4254. [CrossRef]
32. Li, S.; Liu, H.; Wu, R.; Cai, J.; Xi, G.; Jiang, F. Prediction of Spontaneous Imbibition with Gravity in Porous Media Micromodels. *J. Fluid Mech.* **2022**, *952*, A9. [CrossRef]
33. Gu, Q.; Zhang, J.; Liu, H.; Wu, L. Numerical Study of Droplet Behavior Passing through a Constricted Square Channel. *Phys. Fluids* **2023**, *35*, 076611. [CrossRef]
34. Fu, X.; Ba, Y.; Sun, J. Numerical Study of Thermocapillary Migration Behaviors of Droplets on a Grooved Surface with a Three-dimensional Color-gradient Lattice Boltzmann Model. *Phys. Fluids* **2021**, *33*, 062108. [CrossRef]
35. Liu, Y.; Feng, J.; Min, J.; Zhang, X. Homogenized Color-gradient Lattice Boltzmann Model for Immiscible Two-phase Flow in Multiscale Porous Media. *J. Appl. Phys.* **2024**, *135*, 184701. [CrossRef]
36. Ba, Y.; Liu, H.; Sun, J.; Zheng, R. Color-gradient Lattice Boltzmann Model for Simulating Droplet Motion with Contact-angle Hysteresis. *Phys. Rev. E* **2013**, *88*, 043306. [CrossRef] [PubMed]
37. Ba, Y.; Liu, H.; Sun, J.; Zheng, R. Three Dimensional Simulations of Droplet Formation in Symmetric and Asymmetric T-junctions Using the Color-gradient Lattice Boltzmann Model. *Int. J. Heat Mass Transf.* **2015**, *90*, 931–947. [CrossRef]
38. Guo, Z.; Zheng, C.; Shi, B. Discrete Lattice Effects on the Forcing Term in the Lattice Boltzmann Method. *Phys. Rev. E* **2002**, *65*, 046308. [CrossRef]
39. Latva-Kokko, M.; Rothman, D.H. Diffusion Properties of Gradient-based Lattice Boltzmann Models of Immiscible Fluids. *Phys. Rev. E* **2005**, *71*, 056702. [CrossRef]
40. Reis, T.; Phillips, T. Lattice Boltzmann Model for Simulating Immiscible Two-phase Flows. *J. Phys. A-Math. Theor.* **2007**, *40*, 4033–4053. [CrossRef]

Disclaimer/Publisher's Note: The statements, opinions and data contained in all publications are solely those of the individual author(s) and contributor(s) and not of MDPI and/or the editor(s). MDPI and/or the editor(s) disclaim responsibility for any injury to people or property resulting from any ideas, methods, instructions or products referred to in the content.